Al_2O_3-Assisted Hierarchical Ni–Al Surface Alloying for Scalable Fabrication of Nano-Roughened Ni Foam Cathodes with Superior HER Activity and Durability in Alkaline Water Electrolysis

Jeongha Kim [a, b †], Hae In Lee [a], Seonghee Kim [a], Seongmin Park [a], Hee Soo Kim[a], Se-Hun Kwon[b], and Dong-Ha Lim[a,c*]*

[a]Low Carbon Energy Group, Korea Institute of Industrial Technology, Ulsan, 44413, Republic of Korea

[b]Institute of Materials Technology, Pusan National University, Busan 46241, Republic of Korea

[c]Graduate School of Hydrogen & Next Energy Convergence, Pusan National University, Busan 46241, Republic of Korea

[†] These authors contributed equally to this work.

*Corresponding author: sehun@pusan.ac.kr, dongha4u@kitech.re.kr

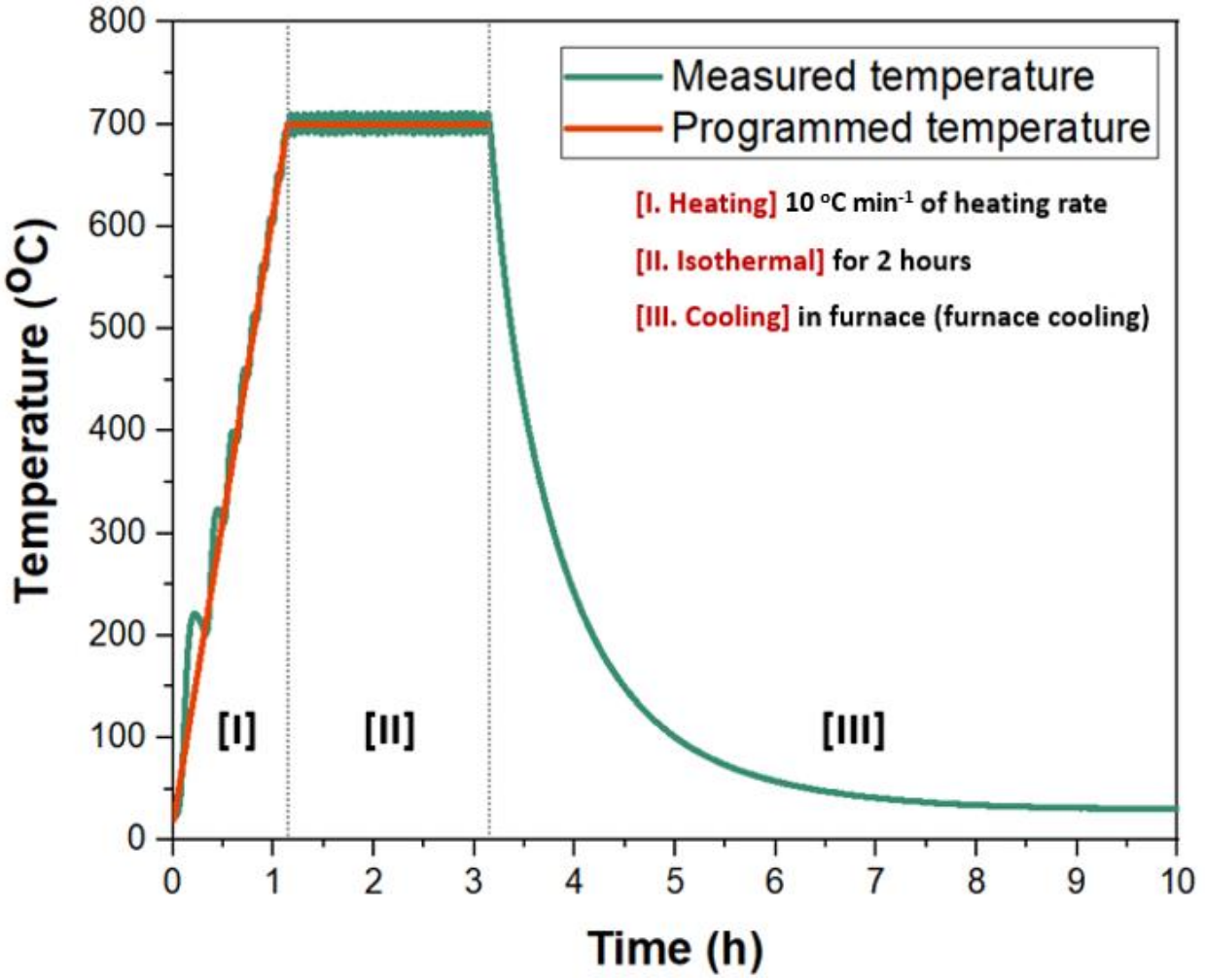

Fig. S1 Programmed temperature profile for the thermal alloying heat treatment (10 °C min^{-1} ramp to 700 °C, 2 h dwell, followed by natural cooling).

Fig. S1 compares the programmed temperature profile for the alloying heat-treatment process with the experimentally measured temperature profile. The thermal process comprised three distinct stages: (i) linear ramping at a rate of 10 °C min^{-1}, (ii) isothermal dwelling at 700 °C for 2 h, and (iii) natural furnace cooling. The measured temperature data exhibited excellent agreement with the programmed curve, validating the stability and reproducibility of the thermal control system employed in this study.

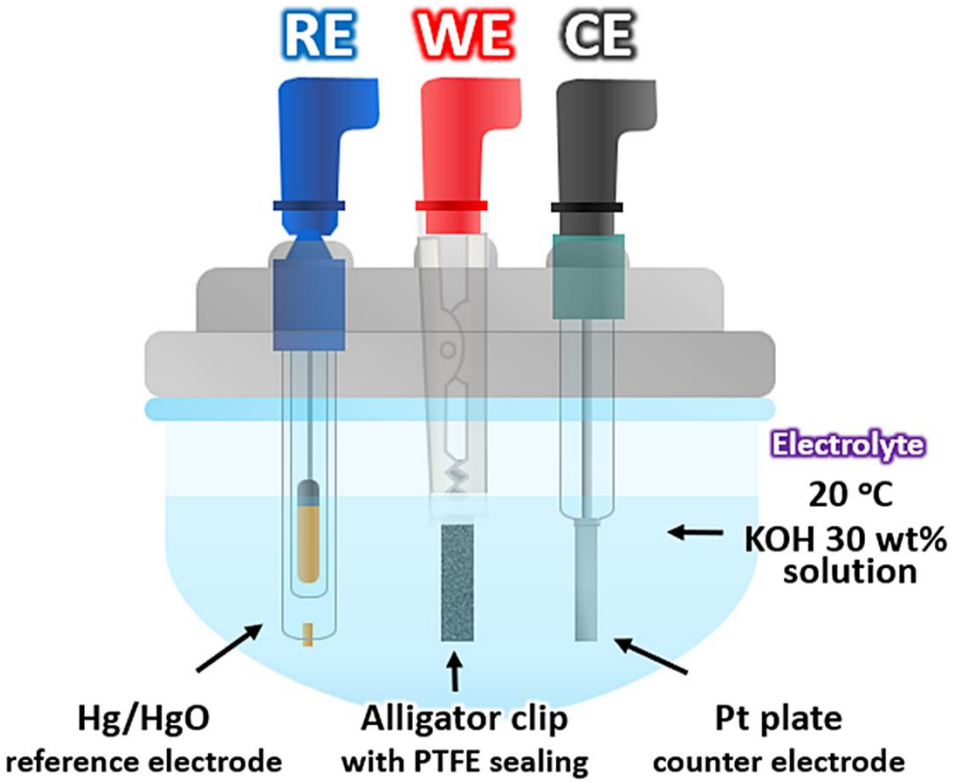

Fig. S2 Schematic illustration of the three-electrode configuration for HER measurements (working electrode: 1 × 1 cm^2, reference electrode: Hg/HgO, counter electrode: Pt) in 30 wt.% KOH at 20 °C, with all potentials referenced to the RHE.

Fig. S2 illustrates the three-electrode electrochemical cell configuration used for evaluating HER performance. The working electrode (WE) was secured using an alligator clip, and its active geometric area was defined as 1 × 1 cm^2 by masking with polytetrafluoroethylene (PTFE) tape. A Hg/HgO electrode and a platinum (Pt) plate were used as the reference electrode (RE) and counter electrode (CE), respectively. A 30 wt.% KOH aqueous solution served as the electrolyte, and all measurements were performed at 20 °C. The measured potentials were converted to the reversible hydrogen electrode (RHE) scale (E_{RHE}).

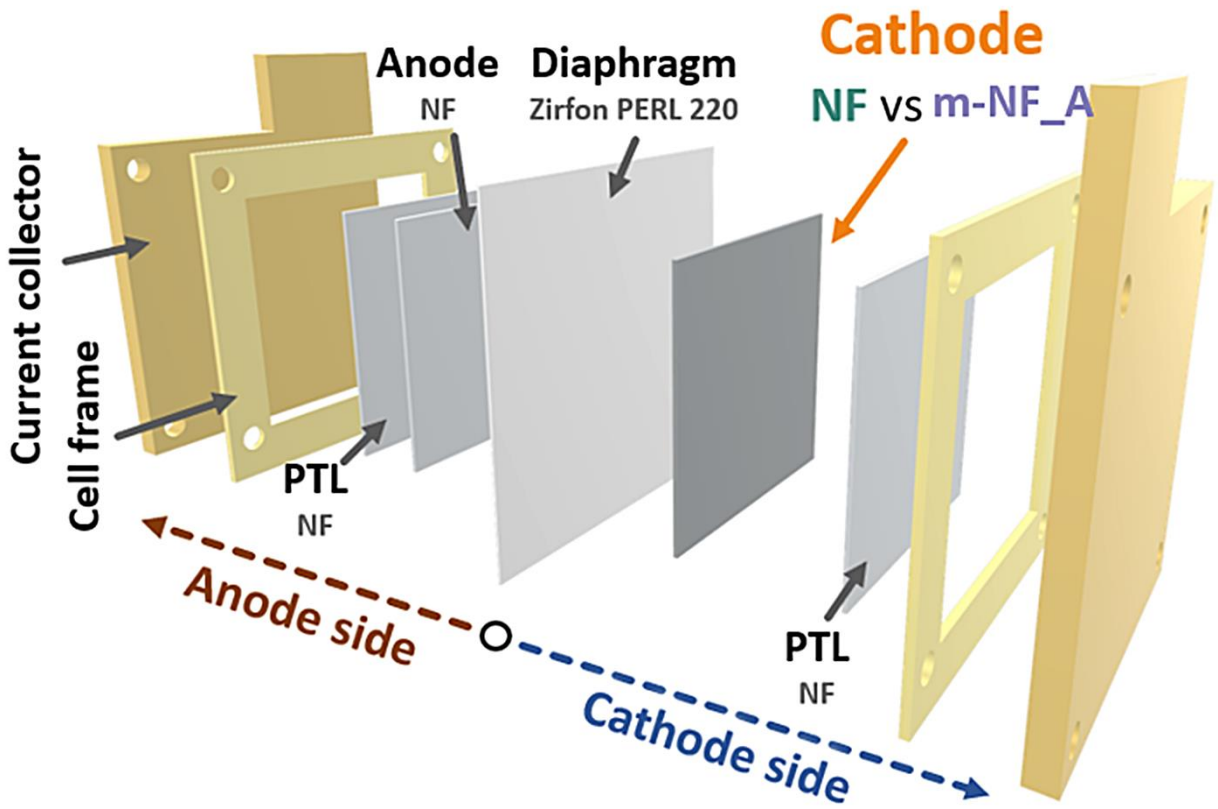

Fig. S3 Schematic illustration of the zero-gap alkaline water electrolysis single-cell configuration (cathode: NF or m-NF_A; anode: Ni foam; diaphragm: Zirfon PERL 220) operated in 30 wt.% KOH at 80 °C.

Fig. S3 illustrates the zero-gap alkaline water electrolysis single-cell configuration used for full-cell performance evaluation. The cell assembly comprises a cathode, an anode, and a diaphragm. On the cathode side, m-NF_A (or pristine NF as a reference) was used; the anode consisted of pristine NF. Porous transport layers (PTLs) were incorporated to facilitate uniform current distribution and effective mass transport. A Zirfon PERL 220 diaphragm was positioned between the electrodes to enable efficient ionic transport while suppressing gas crossover. A 30 wt.% KOH aqueous solution served as the electrolyte, and the operating temperature was maintained at 80 °C.

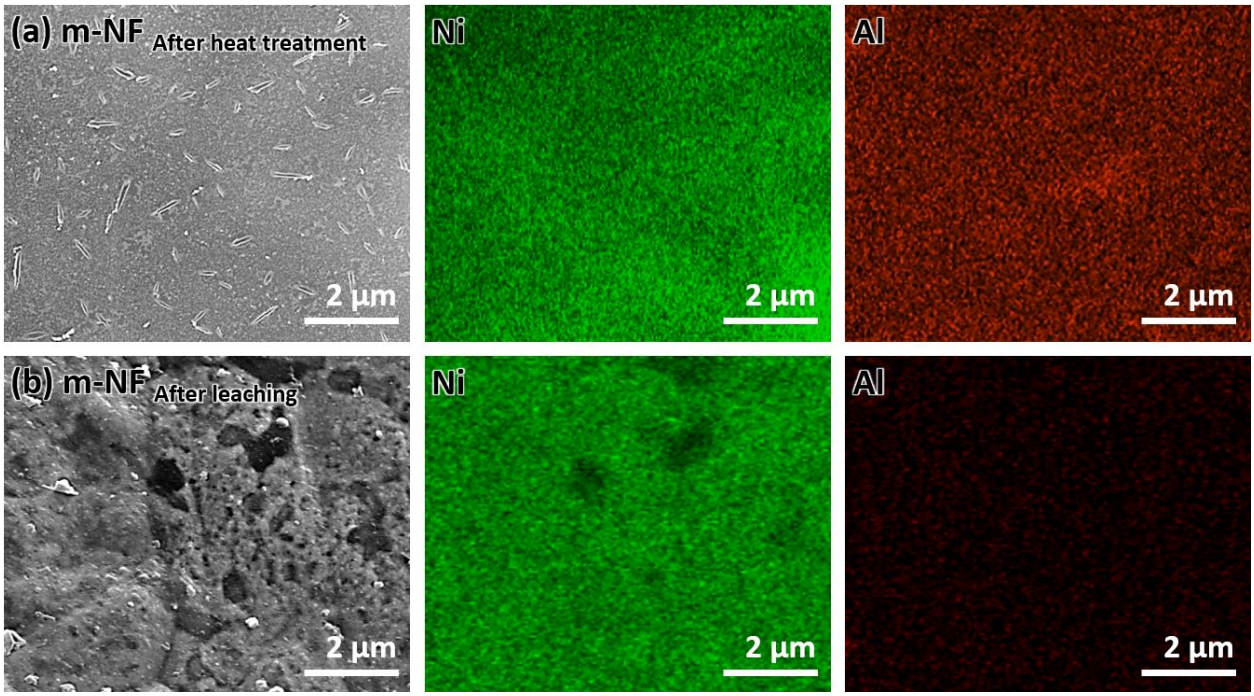

Fig. S4 EDS elemental mapping of m-NF (Al-PEG route) (a-c) after heat treatment and (d-f) after alkaline leaching, showing the formation of Ni-Al interphases after heat treatment and selective removal of Al after leaching.

Fig. S4 presents EDS elemental mapping results comparing the surface compositional distributions of the m-NF electrode before and after alkaline leaching. Following heat treatment, both Ni and Al signals are uniformly detected across the surface, confirming the distribution of Al-containing species on the Ni foam during thermal alloying. In contrast, after selective alkaline leaching, the Al signal is significantly diminished to trace levels, while the Ni signal remains pervasive and uniformly distributed, validating selective Al dissolution and exposure of a Ni-rich skeletal framework. These EDS mapping results corroborate the effective dealloying behaviour of m-NF, in agreement with the structural and topographical evolution observed by SEM.

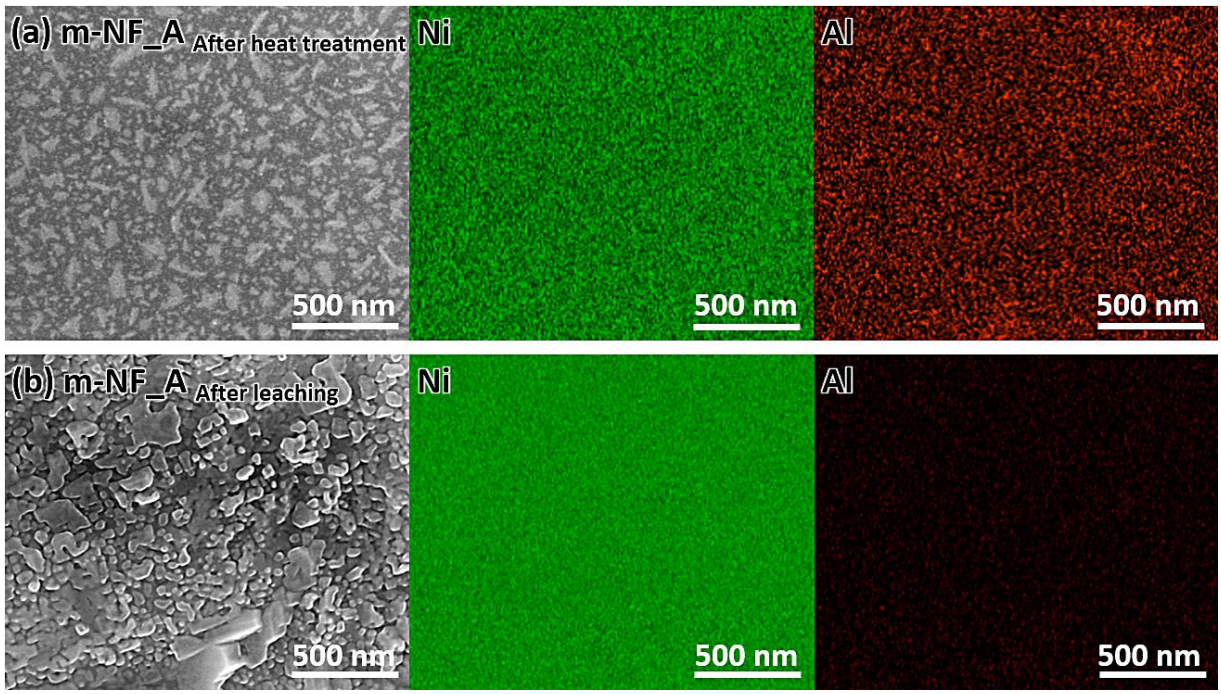

Fig. S5 EDS elemental mapping of m-NF_A (Al-Al_2O_3-PEG route) (a-c) after heat treatment and (d-f) after alkaline leaching, confirming dealloying-driven Ni enrichment and the development of a roughened porous framework.

Fig. S5 presents EDS elemental mapping results comparing the surface compositional states of the m-NF_A electrode before and after alkaline leaching. Following heat treatment (Fig. S5a), Ni and Al signals are uniformly detected across the surface, confirming incorporation of Al-containing species via slurry coating and thermal alloying. In contrast, after selective alkaline leaching (Fig. S5b), the Al signal is significantly diminished to trace levels, while the Ni distribution becomes more prominent, validating selective Al dissolution and exposure of a Ni-rich skeletal framework. The hierarchical roughness observed by SEM after leaching is attributed to surface reconstruction triggered by Al removal, which is intrinsically linked to formation of the secondary nano-textured surface. These findings support the increased electrochemically active surface area (ECSA) and enhanced HER performance of m-NF_A.

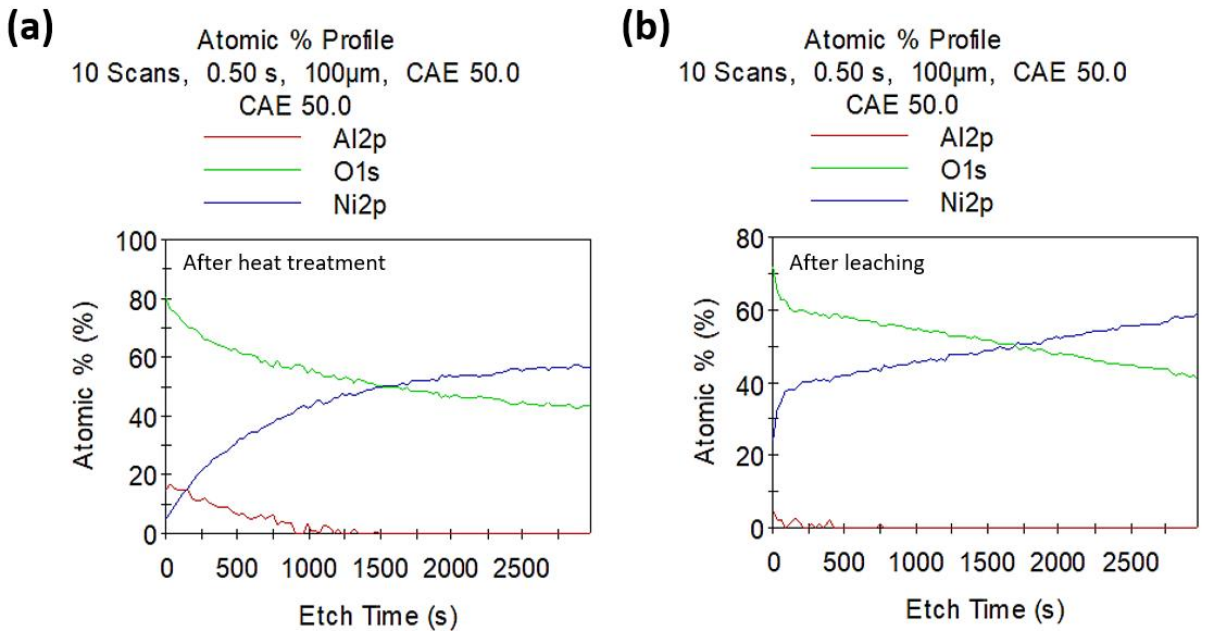

Fig. S6 XPS depth profiles of the m-NF_A electrode (a) after heat treatment and (b) after alkaline leaching.

Fig. S6 presents the XPS depth profiles of the m-NF_A electrode obtained (a) after heat treatment and (b) after alkaline leaching. Following the thermal alloying process, a distinct Al 2p signal is observed in the near-surface region, reflecting the presence of Al-containing species incorporated during the coating and annealing stages. In contrast, after selective alkaline leaching, the Al 2p signal is markedly reduced to below the detection limit across the entire depth profile, with only weak, discontinuous, and noise-like signals being detected. This depth-dependent behaviour is fundamentally different from literature-reported depth profiles for systems where continuous films or coherent layers are present, which typically exhibit sustained signal evolution as a function of sputtering depth [1,2]. The profiles further illustrate a gradual increase in the Ni signal intensity with increasing etching time, consistent with the progressive exposure of a Ni-rich skeletal framework following the rigorous dealloying process. After alkaline leaching, the Al 2p signal is reduced to below the detection limit across the depth profile, with only weak, discontinuous, noise-like signals.

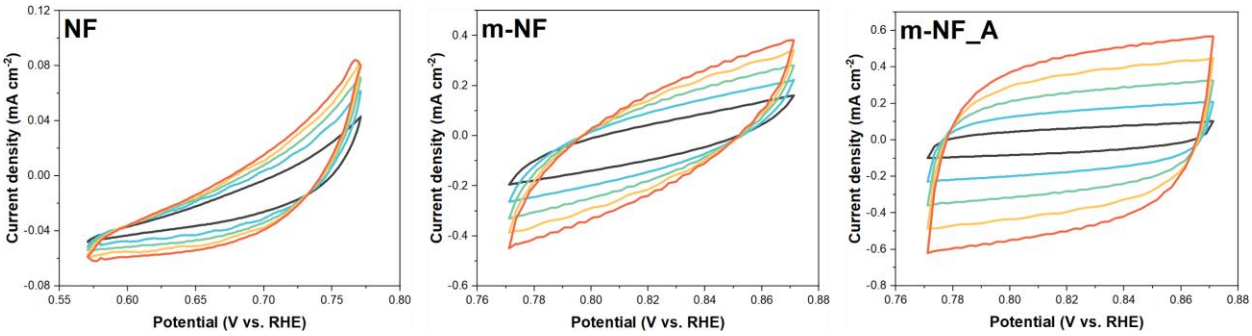

Fig. S7 Cyclic voltammograms of NF, m-NF, and m-NF_A recorded in the non-Faradaic region in 30 wt.% KOH, used to estimate the double-layer capacitance (C_{dl}). The m-NF_A electrode exhibits the highest capacitive current (C_{dl} = 104.2 mF cm^{-2}), consistent with the enlarged ECSA.

Fig. S7 illustrates cyclic voltammetry (CV) results for pristine NF, m-NF, and Al_2O_3-mediated m-NF_A. All measurements were performed within the non-faradaic potential region in 30 wt.% KOH. The magnitude of the capacitive current response is proportional to the electrochemical double-layer capacitance (C_{dl}), which serves as a proxy for the available surface area. Among the tested samples, m-NF_A exhibited the most pronounced current response, indicating that Al_2O_3 incorporation increased surface roughness and active-site density, thereby enhancing the electrochemically active surface area (ECSA).

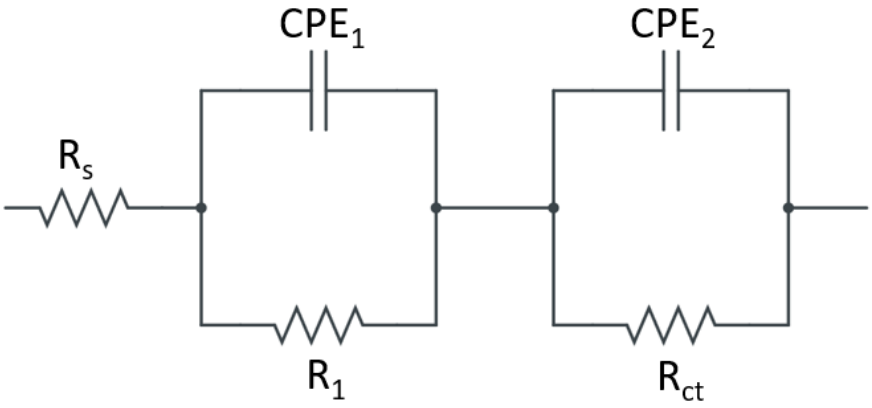

Fig. S8 Equivalent circuit model used to fit EIS Nyquist plots (series R_s with two parallel R_{CPE} elements).

Fig. S8 shows the equivalent circuit model used to fit EIS data and interpret impedance characteristics at the electrode-electrolyte interface. The circuit comprises a series resistance (R_s) connected to two parallel resistance-constant phase element (R_{CPE}) units in series. R_s accounts for the total ohmic resistance derived from the electrolyte, diaphragm, and current collectors.

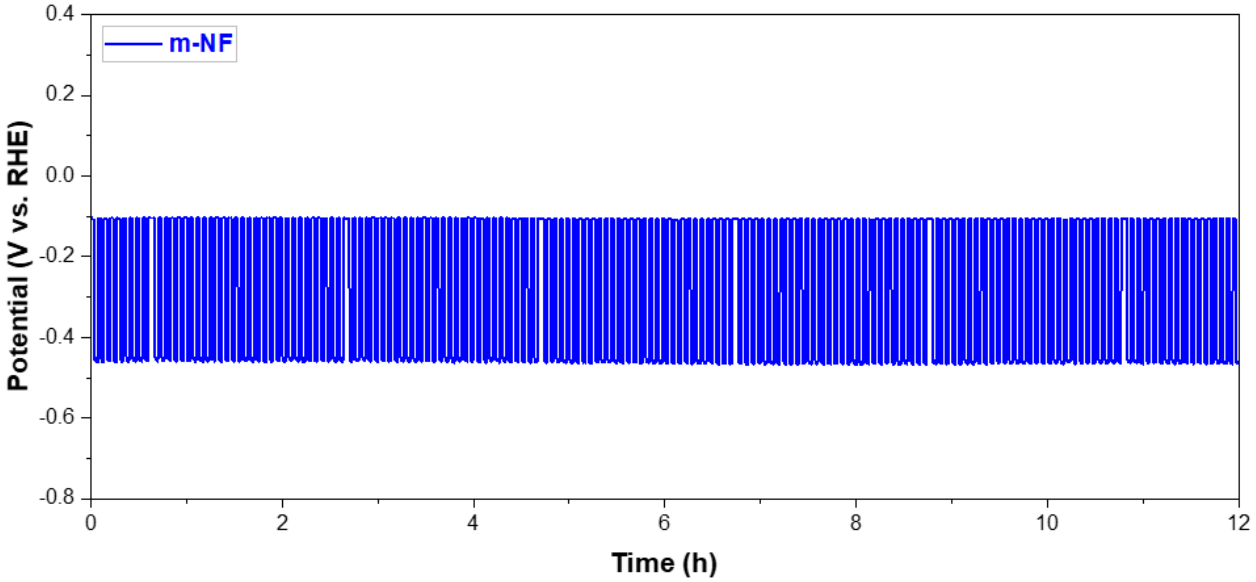

Fig. S9 Additional HER durability evaluation of m-NF under the same AST protocol used in the main text: alternating current densities of -10 and -400 mA cm^{-2} over 360 cycles (12 h).

Fig. S9 presents accelerated stress test (AST) results of the m-NF electrode, obtained by dynamic load cycling between -10 and -400 mA cm^{-2} for a total duration of 12 h (360 cycles). The potential response of m-NF is robust and reproducible throughout the testing period, with no significant potential drift or abrupt fluctuations during repeated current switching.

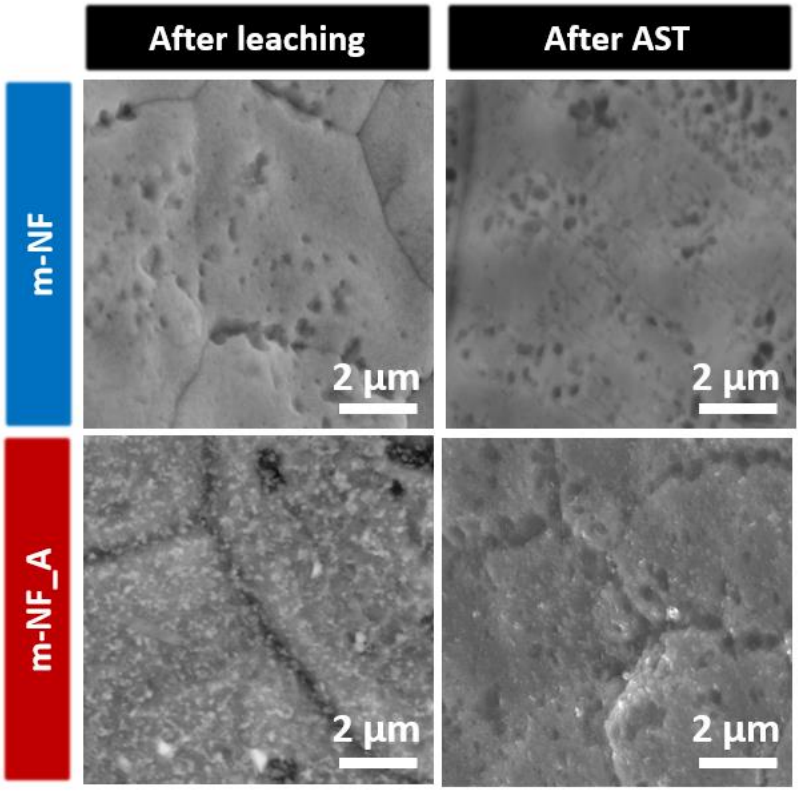

Fig. S10 Post-AST SEM images of the surface-modified electrode (after -10/-400 mA cm^{-2} cycling for 360 cycles, 12 h), showing no apparent structural collapse or severe coarsening of the porous framework.

Fig. S10 presents SEM images of m-NF and m-NF_A after selective alkaline leaching and subsequent accelerated stress testing (AST). No evidence of structural collapse, severe grain coarsening, or pore blockage is observed, confirming preservation of the porous Ni skeletal framework after cycling.

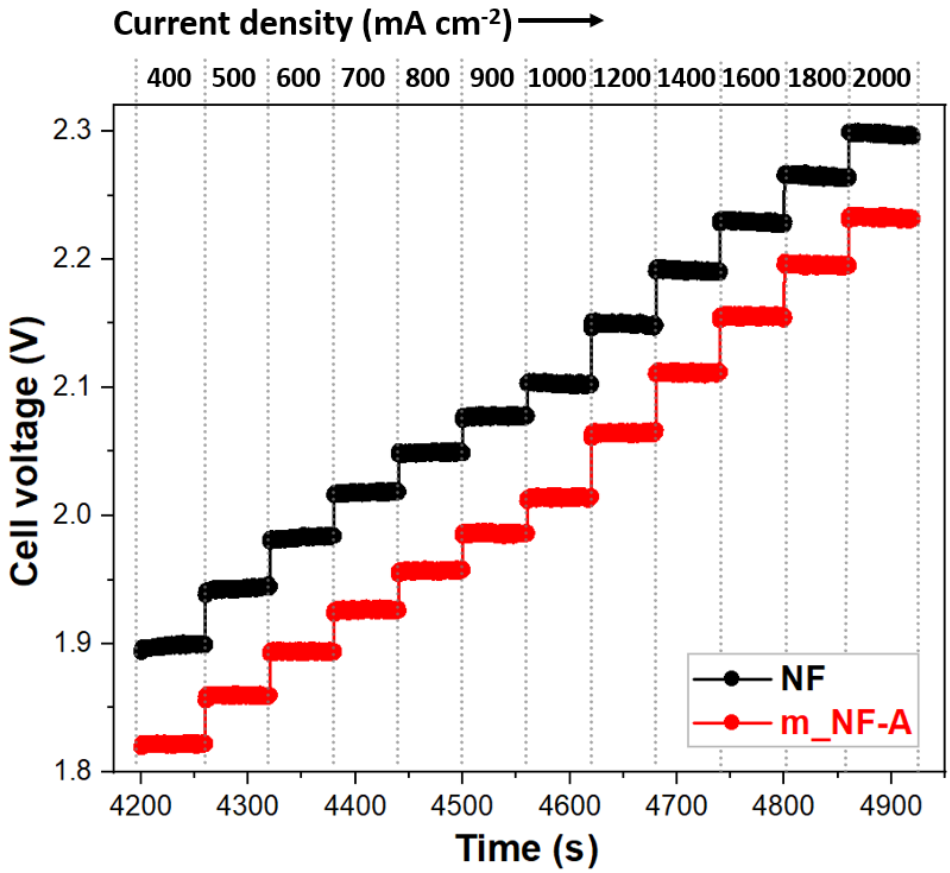

Fig. S11 Constant-potential (CP) / load-following measurements of the alkaline water electrolysis single cell in 30 wt.% KOH at 80 °C, highlighting stable operation under high current densities (as specified in the main text).

Fig. S11 presents chronopotentiometry (CP) profiles of pristine NF and surface-modified m-NF_A recorded at high current densities ranging from 400 to 2,000 mA cm^{-2}. Measurements were performed using the alkaline water electrolysis single-cell configuration illustrated in Fig. S3, where the voltage response and load-following capability were evaluated as a function of current density.

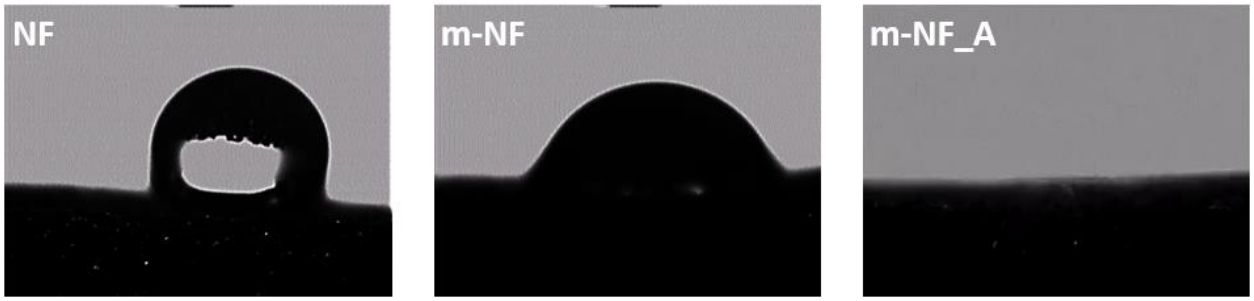

Fig. S12 Static water contact-angle images of NF, m-NF, and m-NF_A, demonstrating the near-zero contact angle (superhydrophilicity) of m-NF_A. Time-dependent wetting/bubble-release behaviour under identical observation conditions is provided in Movies S1-S3.

Fig. S12 presents optical images of the initial water contact angles for pristine NF, m-NF, and m-NF_A immediately upon deposition of a deionized water droplet. The pristine NF electrode exhibits a relatively high contact angle, indicating limited wettability and poor electrolyte affinity. In contrast, m-NF shows a significantly reduced initial contact angle, reflecting enhanced hydrophilicity induced by skeletal surface modification. Notably, m-NF_A displays almost instantaneous spreading of the water droplet with a near-zero contact angle, demonstrating superhydrophilic surface characteristics. This pronounced wetting behaviour is primarily attributed to hierarchical surface modification, which synergistically increases both surface roughness and surface energy. Such superhydrophilicity enhances electrolyte affinity at the electrode-electrolyte interface, promotes formation of a continuous liquid film, alleviates bubble pinning, and facilitates rapid bubble detachment during vigorous gas-evolving reactions. Time-dependent wetting behaviour is provided in Movies S1-S3.

Movies S1-S3 Time-dependent wetting/spreading behaviour immediately after deposition of a deionized water droplet for (S1) pristine NF, (S2) m-NF, and (S3) m-NF_A, corresponding to Fig. S12.

- **Movie S1** High-speed video recording of interfacial wetting and gas-bubble detachment behaviour on NF under the same observation conditions used for the comparative experiment in this study.
- **Movie S2** High-speed video recording of interfacial wetting and gas-bubble detachment behaviour on m-NF under identical conditions.
- **Movie S3** High-speed video recording of interfacial wetting and gas-bubble detachment behaviour on m-NF_A, showing earlier bubble release consistent with its superhydrophilic surface (see Fig. S12).

Table S1 Comparison of HER performance of representative Ni-based catalysts/electrodes in alkaline electrolytes, including the overpotential at 100 mA cm^{-2} and key kinetic parameters, highlighting the competitiveness of m-NF_A.

ALKWE					
Catalysts	**Substrate**	**Electrolyte**	**C_{dl} (mF cm^{-2})**	**Overpotentials @100 mA cm^{-2} (mV)**	**References**
Al/Al_2O_3	Ni foam	30 wt.% KOH	104.2	157.8	**This work**
Al	Ni foam	30 wt.% KOH	32.5	264.5	**This work**
n.a	Ni foam	1.0 M KOH	16.1	172.0	[4]
Ni/Al	Ni plate/foam	1.0 M KOH	44.3	201.2	[5]
Co_3O_4	Ni wire mesh	1.0 M KOH	53.8	136.0	[6]
CoNiP	porous Ni substrate	1.0 M KOH	53.5	118	[7]
Zn/Al	Ni plate	1.0 M KOH	36.99	195.4	[8]
NiFe	Raney Ni substrate	6.0 M KOH	110.6	93.51	[9]
$Ni(OH)_2$	Ni mesh	1.0 M KOH	12.8	163.0	[10]
WMo-CoP	Ni mesh	1.0 M KOH	44.8	114.0	[11]

Reference

[1] M. A. Baker, S. R. Bacon, S. J. Sweeney, S. J. Hinder, A. Bushell, T. S. Nunney and R. G. White, *Appl. Surf. Sci.*, 2024, **654**, 159405-15917.

[2] A. S. Rácz and M. Menyhard, *Sci. Rep.*, 2024, **14**, 18497-18507.

[3] J. E. Kim, K. K. Bae, C. S. Park, S. U. Jeong, K. H. Baik, J. W. Kim, K. S. Kang, K. B. Lee and Y. H. Kim, *J. Ind. Eng. Chem.*, 2019, **70**, 160-168.

[4] Z. Zhu, Y. Lin, P. Fang, M. Wang, M. Zhu, X. Zhang, J. Liu, J. Hu and X. Xu, *Adv. Mater.*, 2024, **36**, 2307035-2307045.

[5] W.-B. Han, I.-S. Kim, M. Kim, W. C. Cho, S.-K. Kim, J. H. Joo, Y.-W. Lee, Y. Cho, H.-S. Cho and C.-H. Kim, *Electrochim. Acta*, 2021, **386**, 138458-13845.

[6] C. Li, X. Luo, Y. Wang, M. Zhu, D. Li, S. Guo, W. Wang and X. Xu, *Adv. Sci.*, 2025, **12**, e08013-e08020.

[7] Z. Xu, S. Li, W. Lu, X. Dou, Y. Wu, J. Zeng, Y. Dou, J. Zhang, J. Wei and L. Yu, *Fuel*, 2023, **348**, 128400-128407.

[8] Y.-I. Choi, E.-C. Wang and H.-A. Kim, *Int. J. Hydrogen Energy*, 2025, **165**, 150894-150901.

[9] Y. Wang, F. Chen, Z. Zhao, Y. Zhang, S. Sun, S. Song, T. Wang, Y. Yuan, J. Zhou and F. Gao, *Nanoscale*, 2024, **16**, 19844-19855.

[10] S. Diao, T. Wang, W. Kuang, S. Yan, X. Zhang, M. Chen, Y. Liu, A. Tan, T. Yang and J. Liu, *Chem. Eng. J.*, 2025, **504**, 158738-158746.

[11] G. Xu, M. Xing, Z. Qiao, M. Han, Y. Wu, S. Wang and D. Cao, *Adv. Energy Mater.*, 2025, **15**, 2500926-2500938.